ACS APPLIED MATERIALS & INTERFACES

www.acsami.org Research Article

Taiwan Rhinoceros Beetle-Inspired Impact-Resistant Structures as Recoverable Antireflection Coatings

Bo-Han Zeng, Shang-Hsuan Lu, Hsiang-Wen Hsueh, Cai-Yin Fang, Shin-Hua Lin, Zi-Xuan Chen, Ya-Lien Cheng, Yu-Fang Wang, Chia-Feng Lin, Rong-Ho Lee, Hui-Ping Tsai,* and Hongta Yang*

Cite This: *ACS Appl. Mater. Interfaces* 2025, 17, 55294−55306 Read Online

ACCESS | Metrics & More | Article Recommendations | Supporting Information

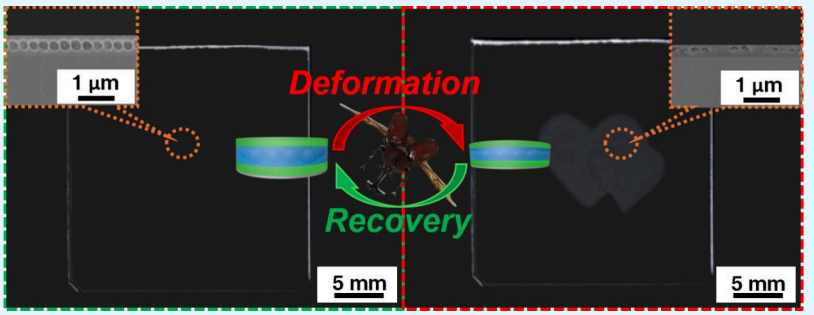

ABSTRACT: Antireflective structures have been widely used to suppress the light reflection occurring on optical lenses, optical devices, and photovoltaic cells. Nevertheless, most of the structures are highly susceptible to mechanical damage, which significantly diminishes their antireflection performance. Bioinspired by the impact-resistant structures found on the Taiwan rhinoceros beetle forewings, shape memory polymer-based sandwich structures are engineered to serve as an antireflection coating. These sandwich structures, templated from self-assembled monolayer silica colloidal crystals, establish a refractive index transition at the air/substrate interface and hence exhibit broadband antireflective characteristics. Moreover, the presence of porous structures facilitates the dissipation of impact energies to protect the substrate underneath. Once the structures are damaged, the stimuli-responsive structures can even recover their original configurations under ambient conditions. Furthermore, the dependence of the structural geometry of the sandwich structure on the antireflective functionality and impact resistance is systematically studied in this research.

KEYWORDS: *antireflective structures, taiwan rhinoceros beetles, impact resistance, sandwich structures, self-assembly, recoverability*

INTRODUCTION

Fresnel reflection appears as light propagates through an interface between two different media with a refractive index mismatch.[1] This light reflection inevitably causes degraded visible transmittance, diminished contrast, and veiling glare in optical instruments and appliances. To mitigate these visual impairments, a broad spectrum of single-layer and multilayer antireflection coatings has been utilized to generate destructive interferences, which further suppress the light reflection.[2−6] However, the development of conventional antireflection coatings is considerably hindered by the limited availability and high cost of low-refractive-index materials. To tackle such challenges, various inorganic hollow materials are employed to introduce micrometer-scale air cavities and thus reduce the effective refractive indices of the coatings.[7−9] Although the refractive index on demand can be straightforwardly achieved through controlling the porosity of the matrix, the application of micrometer-scale voids inevitably induces light scattering, thereby significant reducing optical transmittance. In addition, the random distribution and limited structural control of pores in these coatings lead to inhomogeneous refractive index profiles, resulting in veiling glare and diminished optical contrast. Besides that, the mass production of inorganic hollow materials is impeded by manufacturing complexities and process inefficiencies. Most current fabrication processes involve multiple steps and extensive use of surfactants, which adversely affect the mechanical properties of the resulting coatings.[10,11]

Over more than 400 million years of natural selection and adaptation processes, insects have evolved diverse surface architectures to prevent being tracked by predators. Take moths as an instance; the presence of subwavelength-scale structures on their compound eyes establishes a smooth gradient in refractive index, allowing for the minimization of light scattering and the suppression of optical reflection.[12]

Received: August 12, 2025
Revised: September 11, 2025
Accepted: September 11, 2025
Published: September 19, 2025

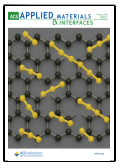

Beyond that, a variety of antireflective structures are found on insect wings, including but not limited to glasswing butterfly wings, leafhopper wings, cicada wings, and dragonfly wings.[13−17] Drawing inspiration from these natural species, a range of nipple-shaped structure arrays, conical structure arrays, soccer ball-like structure arrays, dome-shaped structure arrays, and pyramid-like structure arrays, developed by exploiting photolithography-based fabrication technologies, are adopted as antireflective structures.[18−24] Unfortunately, most photolithography-based methodologies are restricted to the necessity of sophisticated instruments, accompanied by costly and complicated fabrication processes. To overcome these limitations, bottom-up fabrication technologies, such as block copolymer self-assembly methodologies, have been employed to develop antireflective structures.[25,26] However, the as-fabricated subwavelength-scale structures are inherently susceptible to mechanical damage, and it remains a significant challenge to enhance their structural robustness.

By contrast, the exoskeletal elytra of coleopteran insects are utilized as sclerotized sheaths to shield their hindwings and bodies from predation by lizards, birds, and other threats.[27] Notably, the Taiwan rhinoceros beetle elytra, composed of micrometer-scale hollow sandwich architectures, exhibit far superior impact resistance for fights with other beetles over limited resource supplies or mating conflicts.[28,29] The empty spaces within the sandwich-like architectures can be deformed upon the elytra are subjected to external mechanical forces, thereby allowing the beetles to dissipate impact energies efficiently. It is crucial that these damaged configurations and the corresponding mechanical strengths can even gradually return to their original states over time. Bioinspired by the structural features found on the beetle elytra, numerous sandwich composites have been fabricated and adopted as protective coatings.[30−33] In spite of that, the development of beetle-inspired impact-resistant structures with required antireflective capabilities is scarcely documented, primarily owing to the complexities of manufacturing subwavelength-scale hollow sandwich architectures.

Benefiting from the significant progress in nanofabrication technologies, colloidal self-assembly approaches have been extensively employed to construct nanoscale features. In the fabrication procedures, monodispersed colloids are spontaneously organized into well-arranged colloidal crystals, which further act as structural templates to pattern the desired structure arrays. Although the bottom-up fabrication methodologies can be conceived as a launchpad for designing and building hollow sandwich structures, most conventional self-assembly strategies driven by van der Waals forces, gravitational forces, evaporation-induced forces, electric forces, magnetic forces, or chemical stimuli are plagued by low throughput.[34−37] Apart from that, the necessity for subwavelength-scale sandwich structures to possess recoverable impact resistances remains a formidable issue that must be addressed.

Recent advancements in the design and synthesis of shape memory polymers deliver an innovative resolution to address this concern. The shape memory polymer-based structures can undergo an entropy-driven elastic recovery from a deformed state to an original state in response to external physical or chemical stimuli as the temperature exceeds their glass transition temperature.[38−41] Nevertheless, these heat-demanding shape recoveries substantially limit the ultimate performances required for practical applications.[42] In addition, most of the physical stimuli-responsive structural transformations are impeded by prolonged recovery durations, while the chemical stimuli-responsive ones involve the use of designated organic solutions, which are corrosive to other device components and pose risks to human health. Furthermore, the aforementioned reconfigurable features remain constrained by short operational lifespans. Accordingly, there is a pressing need for the development of an advanced structural recovery mechanism.

Herein, we integrate a distinctive shape memory polymer with a roll-to-roll compatible colloidal self-assembly approach to construct subwavelength-scale hollow sandwich structures. In comparison with conventional antireflection coatings, the beetle-inspired antireflective structures can be deformed under external stresses to dissipate impact energies, and hence shall perform enhanced impact resistances. Importantly, the mechanically deformed structures, along with their corresponding antireflection characteristics and impact resistances, can swiftly revert to their original states upon drying of common solvents, such as ethanol, in the ambient environment. It is believed that the recovered antireflective structures provide a platform to realize an array of intelligent optical systems.

EXPERIMENTAL SECTION

Materials. Entomological specimens are provided by the Taiwan Insect Museum. The solvent and reagents applied to synthesize silica spheres, including anhydrous ethanol (200 proof, Merck KGaA), deionized water (18.4 MΩ·cm, Millipore), ammonium hydroxide (27.0%, Merck KGaA), and tetraethyl orthosilicate (≥99.5%, Merck KGaA), are used without any further treatment. Photocurable ethoxylated trimethylolpropane triacrylate (ETPTA) oligomers (SR415, Sartomer), photocurable ethylene glycol diacrylate (EGDA) oligomers (SR610, Sartomer), and their corresponding photoinitiator, 2-hydroxy-2-methyl-1-phenyl-1-propanone (HMPP) (Darocur 1173, BASF), are of reagent quality. A hydrofluoric acid (HF) solution (48.0%, Merck KGaA) is diluted and utilized as a silica-etching agent. Poly(ethylene terephthalate) (PET) films (0.05 cm in thickness, Wisegate Technology) and microscope cover glasses (0.16−0.19 mm in thickness, Thermo Fisher Scientific) are surface-modified with (3-acryloxypropyl)-trichlorosilane (96.0%, Gelest) before use.

Self-Assembly of Close-Packed Silica Colloidal Monolayers. Monodispersed silica spheres, with average diameters of 1 μm, 500, 300, and 150 nm, are synthesized in accordance with the established StÖber approach, respectively.[43] After eliminating unreacted reagents in anhydrous ethanol through 7 dispersion/centrifugation cycles, the spherical silica colloids are well-dispersed in a mixture of photocurable ETPTA oligomers, photocurable EGDA oligomers, and HMPP using an ultrasonic homogenizer (150 VT, BioLogics). The volume ratio of silica colloids, ETPTA oligomers, EGDA oligomers, and HMPP in this silica colloidal suspension is regulated to be 85:3.5:10.5:1. Subsequently, the colloidal suspension is gently dripped onto a beaker of deionized water, in which a poly(ETPTA)/poly(EGDA) (20:1) layer-coated microscope cover glass is immersed beforehand. The poly(ETPTA)/poly(EGDA) (20:1) symbolizes a copolymer consisting of poly(ETPTA) and poly(EGDA) in a ratio of 20:1 by volume. Owing to the surface tension difference between water and the oligomers, these oligomer mixture-covered silica colloids can be arranged spontaneously into an in-plane hexagonal-close-packed ordering on the water surface. A dip-coating system (HO-TH-02MD, Global Analytical) is then introduced to withdraw the copolymer layer-coated glass substrate upward at a constant speed of 2 cm/min, while the Langmuir−Blodgett self-assembled silica colloidal monolayer is transferred onto the copolymer layer. It is worthy to mention that the space between the silica colloidal crystals and the copolymer layer can be filled by the liquiform oligomer mixture during the colloidal deposition procedure. Afterward, the

https://doi.org/10.1021/acsami.5c15999
ACS Appl. Mater. Interfaces 2025, 17, 55294−55306

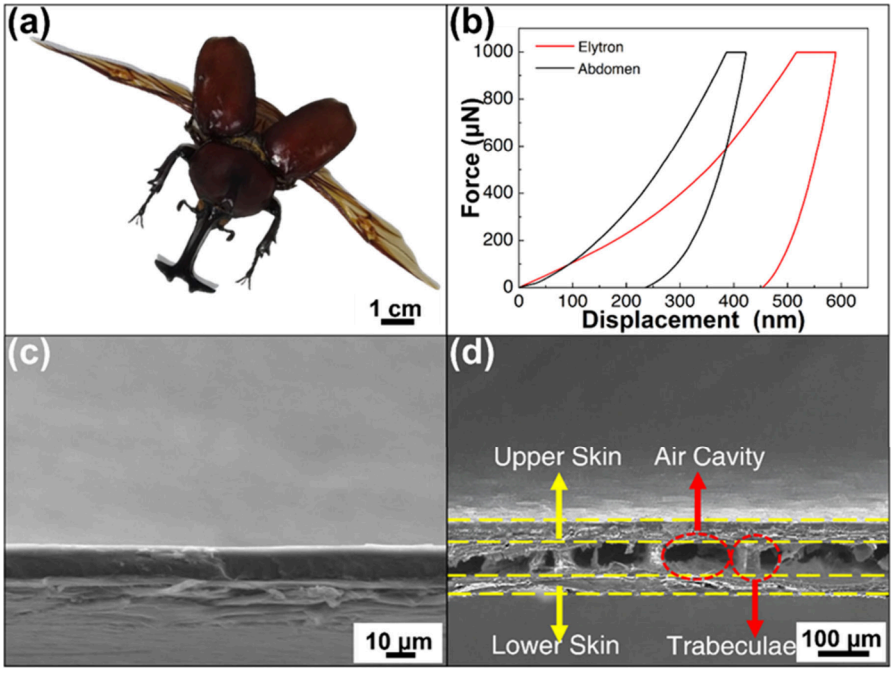

Figure 1. (a) Photographic image of a Taiwan rhinoceros beetle taken under white lighting. (b) Load−displacement curves obtained from nanoindentation tests with maximum loads of 1000 μN on this beetle's abdomen (black curve) and elytron (red curve). Cross-sectional SEM images of (c) the beetle abdomen and (d) the elytron plate.

photocurable oligomers are polymerized under UV illumination for 5 s in a high-powered LED UV-curing chamber (CureUV).

Templating Fabrication of Taiwan Rhinoceros Beetle-Inspired Sandwich Structures. An ETPTA/EGDA oligomer mixture (1:3 in volume ratio) is deposited and spread onto the previously mentioned silica colloidal crystal-coated cover glass utilizing a spin-processor (EDC-650−23B, Laurell Technologies). In the spin-coating process, the glass substrate is progressively spun at 1000 rpm for 2 min, 2000 rpm for 1.5 min, and 3000 rpm for varied durations to ensure that the silica colloids are fully embedded in this oligomer mixture, and to remove any excess mixture. After photopolymerizing the remaining oligomers, the glass substrate can be spin-coated with another poly(ETPTA)/poly(EGDA) (20:1) layer. The templating silica colloids are finally wet-etched using a dilute HF (1.5%) solution to engineer sandwich structures.

Characterization. A digital camera (EOS R10, Canon), an optical microscope (DM4, Leica), and a field-emission scanning electron microscope (SEM) (JSM-IT710HR Schottky, JEOL) are employed to record photographic images, optical microscopy images, and SEM images of the specimens, respectively. The SEM accelerating voltages range from 3 to 5 keV. Before SEM imaging, the specimens are sputter-coated with a thin layer of platinum in a sputter coater (AGB7366, Agar Scientific). The mechanical properties of the specimens are analyzed using a nanomechanical test system equipped with a Berkovich nanoindenter tip (Hysitron TI 990 Triboindenter, Bruker) in ambient conditions. The indentation procedure consists of three sequential steps: loading, holding, and unloading. In the loading step, the applied load is increased to a predetermined maximum value at a constant rate of 20 μN/s. This is followed by a 5-s holding period at the maximum load, which serves to minimize the influence of material creep on the estimated values of modulus and hardness. In the unloading step, the indenter tip is retracted from the specimen at the same rate of 20 μN/s. Normal-incidence optical reflection and transmission spectra over a 400 to 800 nm wavelength range are collected by a high-resolution UV−visible-near-IR spectrometer (HR4000, Ocean Optics) using a deuterium/tungsten/halogen light source (DT-MINI-2-GS, Ocean Optics). The angle of collection is less than 5°, and the light beam spot is controlled to be around 3 mm in diameter on the specimen surface. Absolute reflectivity is determined by comparing the specimen spectrum to a reference spectrum, which is obtained from an aluminum-sputtered silicon wafer. The final absolute reflectivity value is calculated as the average of five measurements taken from different spots on the specimen surface. The mechanical durability of the specimens is evaluated using a Taber abrasion-resistance testing machine (GT-C14A, GESTER). In the abrasion-resistance test (ASTM D 1044), a Taber abrader, equipped with CS-10F wheels, is applied under a 500-g load for a predetermined number of cycles.

RESULTS AND DISCUSSION

Beetles are distinguished by their hardened elytra, which can dissipate impact energies under external stresses to shield the membranous hindwings and abdomens beneath. To verify that, the mechanical behaviors of a Taiwan rhinoceros beetle (*Trypoxylus dichotomus tsunobosonis*) specimen (Figure 1 (a)) are assessed using a nanomechanical test system under a maximum load (F_{max}) of 1000 μN. The load−displacement curves of this beetle abdomen (black curve) and elytron (red curve) are recorded and compared in Figure 1 (b). On the assumption that the adhesion between the nanoindenter tip and the specimen is neglectable, the dissipation impact energy is determined by the enclosed area of each curve, while the corresponding indentation hardness (H) and Young's modulus (E) can be estimated using the Oliver-Pharr indentation data analysis model.[44,45] In this model, $H = \frac{F_{max}}{A}$ and $E = \frac{S\sqrt{\pi}}{2\sqrt{A}}$, of which A refers to the projected surface area in contact with the tip, and S indicates the slope of the unloading curve at the F_{max}. As presented in Table S1, the indentation hardness (0.15 ± 0.03 GPa) and Young's modulus (4.36 ± 0.54 GPa) of this beetle elytron are both lower than the indentation hardness (0.32 ± 0.03 GPa) and Young's modulus (7.06 ± 0.31 GPa) of this beetle abdomen, which are consistent with those reported in previous research.[46,47] The mechanical behavior differences are attributed to the presence of sandwich structures within the elytra. In comparison with the featureless abdomen (Figure 1(c)), it is evident that the beetle elytron consists of a ∼48 μm-

https://doi.org/10.1021/acsami.5c15999
ACS Appl. Mater. Interfaces 2025, 17, 55294−55306

thick upper laminate and a ∼ 43 μm-thick lower laminate, which are bound together by randomly arranged ∼87 μm-high trabeculae (Figure 1(d)). The resulting sandwich structure enables air to occupy the space between the laminates, further providing sufficient space to allow the trabeculae to be temporarily deformed under external stresses. On that account, impact energies applied onto this beetle elytron can be dissipated more efficiently (0.21 ± 0.02 nJ) than the ones applied onto this beetle abdomen (0.09 ± 0.01 nJ), despite the fact that either of them is made of chitin and protein fibers.

Bioinspired by the Taiwan rhinoceros beetle elytra, a Langmuir−Blodgett colloidal self-assembly technology is developed and employed to fabricate sandwich structures (Figure 2). In a typical fabrication process, a microscope cover

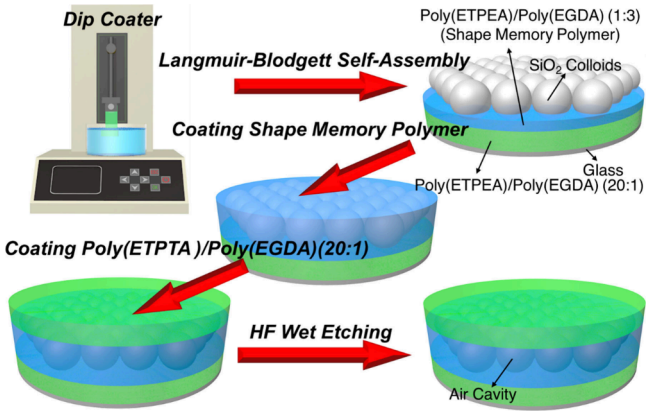

Figure 2. Schematic outline of the fabrication strategy employed to engineer Taiwan rhinoceros beetle-inspired sandwich structures.

glass is sequentially coated with a 250 nm-thick poly(ETPTA)/poly(EGDA) (20:1) layer, a 500 nm-thick poly(ETPTA)/poly(EGDA) (1:3) layer with a self-assembled 500 nm silica colloidal monolayer embedded, and a 250 nm-thick poly(ETPTA)/poly(EGDA) (20:1) layer. Afterward, the silica colloids are wet-etched to create sandwich structures onto the glass substrate. Noteworthily, it is feasible to manipulate the copolymer layer thickness by adjusting the coating parameters; hence, bioinspired sandwich structures with varied configurations can be designed and built (Figure S1). As displayed in Figure 3(a), the self-assembled 500 nm silica colloidal monolayer, deposited onto a poly(ETPTA)/poly(EGDA) (20:1) layer-coated glass substrate, exhibits a brilliant color change over the surface. The structural color is generated by the Bragg diffraction of visible light from the hexagonally close-packed silica colloidal crystals under white light illumination (Figure 3(b)).[48] These 500 nm silica colloids can then be thoroughly embedded through spin-coating with a poly(ETPTA)/poly(EGDA) (1:3) copolymer (Figure 3(c) and (d)). Subsequently, the specimen is spin-coated with another 250 nm-thick poly(ETPTA)/poly(EGDA) (20:1) layer, followed by a wet-etching treatment to remove the templating silica colloids (Figure 3(e) and (f)). It is recognized that the long-range arrangement of air cavities is well-preserved within the resulting sandwich structure. In addition, the thickness ratio of the corresponding upper layer, porous layer, and bottom layer is found to be 1:2:1. As predicted, the bioinspired sandwich structures with varied layer thickness ratios of 1:0.5:1, 1:1:1, and 1:3:1 can be developed as well by regulating

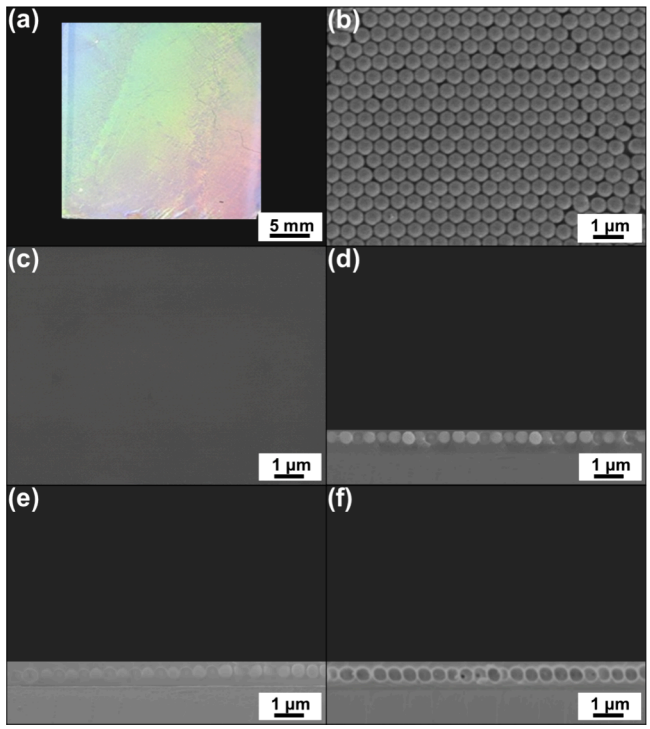

Figure 3. (a) Photographic image of a self-assembled colloidal monolayer, consisting of 500 nm silica spheres, deposited onto a poly(ETPTA)/poly(EGDA) (20:1) layer-coated glass substrate. (b) Top-view SEM image of the specimen in (a). (c) Top-view and (d) cross-sectional SEM images of the silica colloidal crystals spin-coated with poly(ETPTA)/poly(EGDA) (1:3). (e) Cross-sectional SEM image of the silica colloidal crystal/poly(ETPTA)/poly(EGDA) (1:3) composite spin-coated with another poly(ETPTA)/poly(EGDA) (20:1) layer. (f) Cross-sectional SEM image of the corresponding sandwich structure, comprising a 250 nm-thick poly(ETPTA)/poly(EGDA) (20:1) upper layer, a 500 nm-thick poly(ETPTA)/poly(EGDA) (1:3) porous layer, and a 250 nm-thick poly(ETPTA)/poly(EGDA) (20:1) lower layer. The thickness ratio of each copolymer layer is adjusted to be 1:2:1.

the operating conditions of the spin-coating process (Figure S2).

To investigate the dependence of structural configuration on mechanical behaviors, load−displacement curves of featureless poly(ETPTA)/poly(EGDA) coating layers and the aforementioned sandwich structures are conducted under maximum indentation loads of 100 μN. In comparison with the mechanical behaviors of single-layer poly(ETPTA)/poly(EGDA) (20:1) coating or poly(ETPTA)/poly(EGDA) (1:3) coatings, the triple-layer poly(ETPTA)/poly(EGDA) coating, comprising a 250 nm-thick poly(ETPTA)/poly(EGDA) (20:1) upper layer, a 500 nm-thick poly(ETPTA)/poly(EGDA) (1:3) layer, and a 250 nm-thick poly(ETPTA)/poly(EGDA) (20:1) lower layer, exhibits similar indentation hardness (0.12 ± 0.01 GPa), Young's modulus (3.49 ± 0.03 GPa), and dissipation energy (6.72 ± 0.17 pJ) (Figure S3, Figure S4, and Table S2). These results agree well with previous research.[49,50] By contrast, the bioinspired sandwich structures behave with lower indentation hardnesses and Young's moduli (Figure 4 and Table 1). Besides that, it is found that the indentation hardness is gradually decreased from 0.10 ± 0.01 to 0.08 ± 0.01 GPa as the layer thickness ratio of the sandwich structure varies from 1:0.5:1 to 1:2:1, whereas the indentation hardness is increased to 0.09 ± 0.01

https://doi.org/10.1021/acsami.5c15999
ACS Appl. Mater. Interfaces 2025, 17, 55294−55306

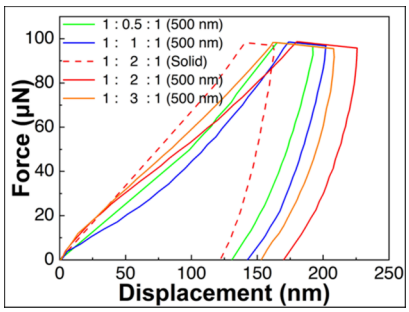

Figure 4. Load−displacement curves obtained from nanoindentation tests with maximum loads of 100 μN on the Taiwan rhinoceros beetle-inspired sandwich structures, templated from 500 nm silica colloidal crystals. The thickness ratio of each layer is adjusted to be 1:0.5:1 (φ = 0.12, green curve), 1:1:1 (φ = 0.20, blue curve), 1:2:1 (φ = 0.30, red curve), and 1:3:1 (φ = 0.36, orange curve), respectively. In comparison, the red dashed curve represents the load−displacement curve of triple-layer solid copolymers, which are with a layer thickness ratio of 1:2:1.

Table 1. Young's Moduli, Hardness, and Dissipation Energies of Taiwan Rhinoceros Beetle-Inspired Sandwich Structures with Varied Layer Thickness Ratios

Sample	Porosity	Experimental / Theoretical Young's Modulus (GPa)	Hardness (GPa)	Dissipation Energy (10^{-12} J)
1:2:1 (Solid)	0	3.49 ± 0.03 / NA	0.12 ± 0.01	6.72 ± 0.17
1:0.5:1 (500 nm)	0.12	2.87 ± 0.11 / 2.92	0.10 ± 0.01	7.68 ± 0.23
1:1:1 (500 nm)	0.20	2.59 ± 0.09 / 2.58	0.09 ± 0.01	7.94 ± 0.16
1:2:1 (500 nm)	0.30	2.17 ± 0.13 / 2.17	0.08 ± 0.01	11.52 ± 0.14
1:3:1 (500 nm)	0.36	2.58 ± 0.17 / 1.93	0.09 ± 0.01	10.63 ± 0.19

GPa once the layer thickness ratio reaches 1:3:1. Crucially, the bioinspired sandwich structures display similar trends in the reduction of their Young's moduli. A minimal Young's modulus of 2.17 ± 0.13 GPa can be achieved on the sandwich structure with a layer thickness ratio of 1:2:1. It is evident that the introduction of larger porosities within the structures results in the formation of even lower indentation hardnesses and Young's moduli. On the contrary, the sandwich structure with a layer thickness ratio of 1:3:1 shall be completely squeezed under the load of 100 μN, thus leading to higher indentation hardness and Young's modulus (Figure S5).

The relation between the porosity of the bioinspired sandwich structure and its corresponding Young's modulus can further be expounded using the Gibson−Ashby model.[50]

$$E_{porous} = E_{solid} \times c(1 - \varphi)^n \quad (1)$$

In this equation, E_{porous} and E_{solid} represent Young's moduli of a structured material with a porosity of φ and the corresponding unstructured material, respectively, while c and n are constants. The φ can be expressed as $\frac{V_{air}}{V_{total}}$, where V_{air} denotes the volume of air cavities per unit volume of the structured material (V_{total}). For the bioinspired sandwich structures, the φ is given by

$$\varphi = \frac{V_{air}}{V_{total}} = \frac{\frac{(4/3)\times\pi\times r^3}{2}}{\frac{\sqrt{3}}{4}\times(2r)^2\times h} = \frac{2\sqrt{3}\pi\times r}{9\times h} \quad (2)$$

, in which r indicates the radius of the air cavity (250 nm), and h refers to the thickness of the sandwich structure. Accordingly, the presence of thinner upper and bottom layers within the sandwich structure generates a larger φ, which further brings about a reduced E_{porous}. To better comprehend the relation between the E_{porous} and φ, the values of $-\ln\left(\frac{E_{porous}}{E_{solid}}\right)$ and $-ln(1-\varphi)$ of these sandwich structures are computed, and their relationship is modeled using a linear regression analysis (Table S3 and Figure S6). In this analysis, the model takes on the following form derived from the eq 1.

$$-\ln\left(\frac{E_{porous}}{E_{solid}}\right) = n \times [-\ln(1-\varphi)] - \ln(c) \quad (3)$$

In view of this, the c (0.99) and n (1.30) are determined, and thereupon the E_{porous} can be theoretically estimated using the eq 1. As summarized in Table 1, the theoretical E_{porous} decreases from 2.92 to 2.17 GPa as the layer thickness ratio of the sandwich structure is altered from 1:0.5:1 to 1:2:1. It is ascertained that these theoretical values match well with the experimental ones, which indicates that sandwich structures with required Young's moduli can be created on demand. Crucially, the reduction in Young's modulus facilitates the

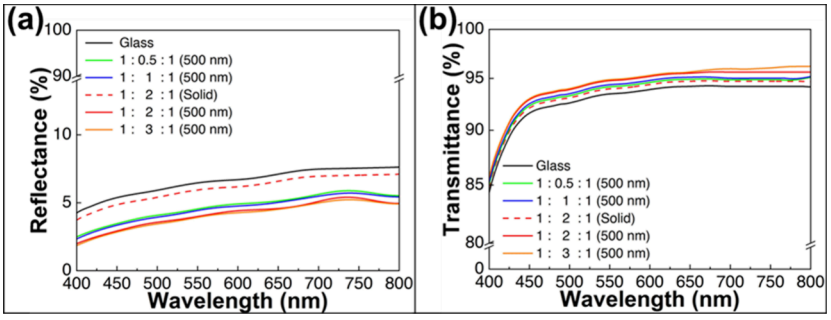

Figure 5. (a) Normal-incidence optical reflection spectra and (b) normal-incidence optical transmission spectra of a bare glass substrate (black curve) and glass substrates coated with Taiwan rhinoceros beetle-inspired sandwich structures. The thickness ratio of each layer is adjusted to be 1:0.5:1 (φ = 0.12, green curve), 1:1:1 (φ = 0.20, blue curve), 1:2:1 (φ = 0.30, red curve), and 1:3:1 (φ = 0.36, orange curve), respectively. In comparison, the red dashed curve represents the optical spectrum of triple-layer solid copolymers, which are with a layer thickness ratio of 1:2:1.

https://doi.org/10.1021/acsami.5c15999
ACS Appl. Mater. Interfaces 2025, 17, 55294−55306

deformation of porous structures, generating a larger projected surface area in contact with the nanoindenter tip (A) and a decreased indentation hardness ($H = \frac{F_{max}}{A}$). The integration of a reduced Young's modulus and a decreased hardness further allows the bioinspired sandwich structure to dissipate impact energies more efficiently. It has been verified that the dissipation energy of the sandwich structure is increased from 7.68 ± 0.23 pJ to 11.52 ± 0.14 pJ as the corresponding porosity (φ) varies from 0.12 to 0.36. Most importantly, the dissipation energy can even be increased by nearly 71.4% in comparison with that of a triple-layer poly(ETPTA)/poly(EGDA) coating (6.72 ± 0.17 pJ).

For evaluating the antireflection capabilities of the Taiwan rhinoceros beetle-inspired sandwich structures, normal-incidence optical reflection and transmission spectra of a bare glass substrate, a triple-layer poly(ETPTA)/poly(EGDA) copolymer-coated glass substrate, and glass substrates coated with these bioinspired sandwich structures are assessed and compared in Figure 5. Owing to the discontinuous refractive index transition at the air/glass interface, the bare glass substrate (black curve) presents an average reflectance of 6.5 ± 0.1% and an average transmittance of 92.5 ± 0.1% in the visible wavelength region ranging from 400 to 800 nm. By comparison, the application of a triple-layer copolymer coating enables the air/glass interface to be replaced by an air/copolymer interface and a copolymer/glass interface. Since the copolymer has a refractive index ($n_{copolymer}$ = 1.47) that lies between those of glass (n_{glass} = 1.52) and air (n_{air} = 1), less light reflection occurs at these interfaces than that at the air/glass interface. As a result, the triple-layer copolymer-coated glass substrate (red dashed curve) displays a lower average reflectance (6.0 ± 0.1%) and a higher average transmittance (93.0 ± 0.1%). Importantly, the specular reflection in the visible spectrum can be further suppressed by introducing these bioinspired sandwich structures. The incorporation of spherical pores even leads to a less steep refractive index transition. It is found that the average reflectance of the sandwich structure-coated glass substrate gradually reduces from 4.6 ± 0.1%, 4.4 ± 0.2%, 4.0 ± 0.2% to 3.9 ± 0.2% as the layer thickness ratio of each sandwich structure varies from 1:0.5:1 (φ = 0.12, green curve), 1:1:1 (φ = 0.20, blue curve), 1:2:1 (φ = 0.30, red curve) to 1:3:1 (φ = 0.36, orange curve), while the corresponding average transmittance is increased from 93.2 ± 0.1%, 93.4 ± 0.2%, 93.8 ± 0.1% to 93.9 ± 0.1%.

Table 2. Average Reflectances and Transmittances of a Bare Glass Substrate, a Triple-Layer Solid Copolymer-Coated Glass Substrate, and Glass Substrates Coated with Taiwan Rhinoceros Beetle-Inspired Sandwich Structures[a]

Sample	Porosity	Experimental / Theoretical	
		R (%)	T (%)
Glass	0	6.5 ± 0.1 / 4.3	92.5 ± 0.1 / 94.7
1:2:1 (Solid)	0	6.0 ± 0.1 / 3.6	93.0 ± 0.1 / 95.4
1:0.5:1 (500 nm)	0.12	4.6 ± 0.1 / 3.1	93.2 ± 0.1 / 95.9
1:1:1 (500 nm)	0.20	4.4 ± 0.2 / 2.9	93.4 ± 0.2 / 96.1
1:2:1 (500 nm)	0.30	4.0 ± 0.2 / 2.5	93.8 ± 0.1 / 96.5
1:3:1 (500 nm)	0.36	3.9 ± 0.2 / 2.4	93.9 ± 0.1 / 96.6

[a]The thickness ratio of each layer is adjusted to be 1:0.5:1, 1:1:1, 1:2:1, and 1:3:1, respectively.

The resulting broadband antireflection performance can be interpreted by adopting the Fresnel equations.[51] In this study, the whole reflectance (R_{total}) is expressed as a function of the refractive indices of air (n_{air}), sandwich structures ($n_{structure}$), and glass (n_{glass}).

$$R_{total} = R_{air/structure} + (1 - R_{air/structure}) \times R_{structure/glass} \quad (4)$$

$$= \left(\frac{n_{air} - n_{structure}}{n_{air} + n_{structure}}\right)^2 + \left(1 - \left(\frac{n_{air} - n_{structure}}{n_{air} + n_{structure}}\right)^2\right) \times \left(\frac{n_{structure} - n_{glass}}{n_{structure} + n_{glass}}\right)^2 \quad (5)$$

$$= \frac{(n_{glass} + n_{structure})^2 \times (n_{structure} - n_{air})^2 + 4 \times n_{structure} \times n_{air} \times (n_{glass} - n_{structure})^2}{(n_{glass} + n_{structure})^2 \times (n_{structure} + n_{air})^2} \quad (6)$$

$$= \frac{(1.52 + n_{structure})^2 \times (n_{structure} - 1)^2 + 4 \times n_{structure} \times (1.52 - n_{structure})^2}{(1.52 + n_{structure})^2 \times (n_{structure} + 1)^2} \quad (7)$$

(4)

, where $n_{structure} = \sqrt{n_{air}^2 \times \varphi + n_{copolymer}^2 \times (1 - \varphi)}$ and $\varphi = \frac{2\sqrt{3}\pi r}{9h}$. As summarized in Table 2, the estimated light reflectance is decreased from 3.1 to 2.4% as the layer thickness ratio of the sandwich structure varies from 1:0.5:1 to 1:3:1. Compared with other sandwich structures, the one with a layer thickness ratio of 1:3:1 possesses a largest φ of 0.36 and a lowest $n_{structure}$ of 1.32, which leads to a minimal reflectance. The transmittances (T) of those glass substrates can further be theoretically calculated using the following equation by assuming that the light absorption (A) is negligible (~1%).

$$T = 1 - R_{total} - A \quad (8)$$

It is evidenced that the light transmissions are enhanced on the sandwich structure-coated glass substrates, and a maximal transmittance of 96.6% shall be achieved as the corresponding layer thickness ratio reaches 1:3:1 (φ = 0.36). Although the as-calculated reflectances and transmittances exhibit similar trends to those experimental values, it is found that the

https://doi.org/10.1021/acsami.5c15999
ACS Appl. Mater. Interfaces 2025, 17, 55294−55306

experimental ones are with even higher average reflectances and lower average transmittances. The impaired antireflective performance is primarily caused by incident light reflection from the 500 nm pores and light refraction within the sandwich structures.

To address the issues, Taiwan rhinoceros beetle-inspired sandwich structures with varied pore sizes are engineered onto cover glasses (Figure S7). Instead of 500 nm silica spheres, silica spheres with diameters of 1 μm, 300 nm, and 150 nm are self-assembled to form close-packed colloidal monolayers, respectively, which are then employed as structural templates to build sandwich structures (Figure S8, Figure 6, and Figure S9). It is worth noting that the layer thickness ratio of each sandwich structure is controlled to be 1:2:1. Therefore, these sandwich structures are with the same φ of 0.30, and shall possess identical antireflection functionalities. As verified in Figure S10, the average reflectances of these sandwich structure-coated glass substrates remain nearly unchanged. Nevertheless, the sandwich structure templated from 1 μm silica colloidal crystals exhibits a much lower average transmittance (79.7 ± 0.7%) in the visible wavelength region, which is attributed to light scattering from the micrometer-scale pores. The considerable light scattering further induces the formation of optical haziness (Figure S11). By contrast, less incident light is scattered from subwavelength-scale pores, and hence, the antireflection performance can be improved by introducing smaller pores within the structures. It has been found that the average transmittance of the sandwich structure templated from 300 nm silica colloidal crystals can reach 94.7%, while an average transmittance of 95.2% is achieved on the sandwich structure templated from 150 nm silica colloidal crystals (Table 3). Although the effective medium theory offers a convenient approximation, significant discrepancies arise between the theoretical and experimental transmittances for structures beyond the visible wavelength scale. To address this issue, a rigorous coupled-wave analysis (RCWA) (DiffractMOD, RSoft Design Group), as established in previous studies, is employed to analyze the optical behaviors of planar waves on the bioinspired sandwich structures.[52−54] In the model, the sandwich structures are composed of hexagonally close-packed pores with diameters of 1 μm, 500, 300, and 150 nm, respectively. The layers are designed with a thickness ratio of 1:2:1. For the purpose of simplifying the present analysis, the imaginary components of the refractive indices are neglected in the simulation, and the refractive indices are treated as wavelength-independent constants, justified by the fact that the materials exhibit minimal dispersion over the spectral range of interest in this study.[52] A sufficient number of spatial harmonics was included to guarantee convergence with an error less than 5%, and all diffraction orders were considered in the calculation. Furthermore, the angle of incidence is fixed at 0°, which ensures that the simulation results are invariant for both transverse-electric and transverse-magnetic polarizations. As shown in Figure S12, the simulated reflection and transmission spectra of the sandwich structure-coated glass substrates are in good agreement with the corresponding experimental results. The findings further indicate that this RCWA is valid for the coating templated from 1 μm silica colloidal crystals.

The pore size effect on the impact resistances of sandwich structures is investigated as well. On account of the presence of thicker upper and bottom layers, the structure templated from 1 μm silica colloidal crystals behaves with a higher indentation hardness (0.09 ± 0.01 GPa) and a higher Young's modulus (2.57 ± 0.23 GPa) in comparison to the mechanical behaviors of the one templated from 500 nm silica colloidal crystals (Figure S13 and Table 4). The integration of higher

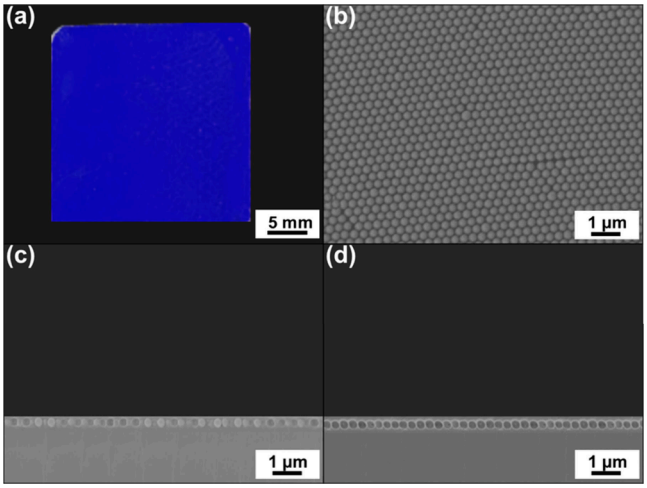

Figure 6. (a) Photographic image of a self-assembled colloidal monolayer, consisting of 300 nm silica spheres, deposited onto a poly(ETPTA)/poly(EGDA) (20:1) layer-coated glass substrate. (b) Top-view SEM image of the specimen in (a). (c) Cross-sectional SEM image of the silica colloidal crystals sequentially spin-coated with a poly(ETPTA)/poly(EGDA) (1:3) layer and a poly(ETPTA)/poly(EGDA) (20:1) layer. (d) Cross-sectional SEM image of the corresponding sandwich structure, comprising a 150 nm-thick poly(ETPTA)/poly(EGDA) (20:1) upper layer, a 300 nm-thick poly(ETPTA)/poly(EGDA) (1:3) porous layer, and a 150 nm-thick poly(ETPTA)/poly(EGDA) (20:1) lower layer.

Table 3. Average Reflectances and Transmittances of a Bare Glass Substrate, a Triple-Layer Solid Copolymer-Coated Glass Substrate, and Glass Substrates Coated with Taiwan Rhinoceros Beetle-Inspired Sandwich Structures[a]

Sample	Porosity	Experimental / Theoretical	
		R (%)	T (%)
Glass	0	6.5 ± 0.1 / 4.3	92.5 ± 0.1 / 94.7
1:2:1 (Solid)	0	6.0 ± 0.1 / 3.6	93.0 ± 0.1 / 95.4
1:2:1 (1 μm)	0.30	4.1 ± 0.4 / 2.5	79.7 ± 0.7 / 96.5
1:2:1 (500 nm)	0.30	4.0 ± 0.2 / 2.5	93.8 ± 0.1 / 96.5
1:2:1 (300 nm)	0.30	4.2 ± 0.1 / 2.5	94.7 ± 0.2 / 96.5
1:2:1 (150 nm)	0.30	3.8 ± 0.1 / 2.5	95.2 ± 0.1 / 96.5

[a]The sandwich structures are templated from 1 μm silica colloidal crystals, 500 nm silica colloidal crystals, 300 nm silica colloidal crystals, and 150 nm silica colloidal crystals, respectively. The thickness ratio of each layer is adjusted to be 1:2:1.

https://doi.org/10.1021/acsami.5c15999
ACS Appl. Mater. Interfaces 2025, 17, 55294−55306

Table 4. Young's Moduli, Hardness, and Dissipation Energies of Taiwan Rhinoceros Beetle-Inspired Sandwich Structures, Templated from Different Silica Colloidal Crystals[a]

Sample	Porosity	Experimental / Theoretical Young's Modulus (GPa)	Hardness (GPa)	Dissipation Energy (10^{-12} J)
1:2:1 (Solid) 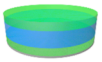	0	3.49 ± 0.03 / NA	0.12 ± 0.01	6.72 ± 0.17
1:2:1 (1 μm) 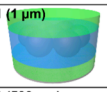	0.30	2.57 ± 0.23 / 2.17	0.09 ± 0.01	8.43 ± 0.26
1:2:1 (500 nm) 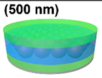	0.30	2.17 ± 0.13 / 2.17	0.08 ± 0.01	11.52 ± 0.14
1:2:1 (300 nm) 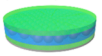	0.30	2.31 ± 0.14 / 2.17	0.08 ± 0.01	10.96 ± 0.17
1:2:1 (150 nm) 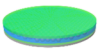	0.30	2.86 ± 0.28 / 2.17	0.11 ± 0.02	7.22 ± 0.13

[a]The thickness ratio of each layer is adjusted to be 1:2:1.

indentation hardness and Young's modulus enables the structure to be less contorted under a maximum indentation load of 100 μN, thus allowing less impact energy to be dissipated (8.43 ± 0.26 pJ). On the other hand, the sandwich structures templated from smaller silica spheres are composed of thinner upper layers, smaller pores, and thinner bottom layers, which facilitate the deformation of porous structures and shall perform improved impact resistances. However, an enhanced impact resistance is not realized on the sandwich structure templated from 300 nm silica colloidal crystals. It is found that this structure behaves with an indentation hardness of 0.08 ± 0.01 GPa, a Young's modulus of 2.31 ± 0.14 GPa, and a dissipation energy of 10.96 ± 0.17 pJ, which are similar to those values of the structure templated from 500 nm silica colloidal crystals. Astonishingly, the sandwich structure templated from 150 nm silica colloidal crystals even displays a declined dissipation energy (7.22 ± 0.13 pJ). The findings further disclose that these 150 nm pores have been thoroughly squeezed under the load of 100 μN. To gain a more comprehensive understanding, nanoindentation tests with maximum loads of 500 μN are applied onto the sandwich structures as stated previously, and the resulting load–displacement curves are compared in Figure S14. As expected, the structures templated from either 150 nm silica spheres or 300 nm silica spheres are wholly deformed under this load, thereby exhibiting slightly higher impact resistances than that of a triple-layer copolymer coating (Table S4). Remarkably, the dissipation energy is increased with the pore size, and a maximal dissipation energy of 97.61 ± 0.86 pJ is achieved on the structure templated from 1 μm silica spheres. It is explicit that the impact resistances under larger loads can be ameliorated by introducing larger pores within the sandwich structures, even though these structures have the same porosity.

To further comprehend the role of structural geometry in the impact resistance, bioinspired sandwich structures with varied pore geometries are developed following the above-mentioned Langmuir–Blodgett approach (Figure S15). In the fabrication process, silica colloidal monolayers are self-assembled using 300 nm silica colloidal suspensions with different colloid volume fractions of 71 vol % and 79 vol %, respectively. Subsequently, the close-packed silica colloidal crystals are deposited onto a poly(ETPTA)/poly(EGDA) (20:1) layer-coated glass substrate, followed by a photopolymerization procedure. It is worth mentioning that the usage of colloidal suspension with a higher colloid volume fraction leads to the formation of less copolymer matrix-embedded silica colloidal crystals, and hexagonally arranged holes with larger openings are therefore generated after wet-etching the silica templates (Figure S16 and Figure 7).

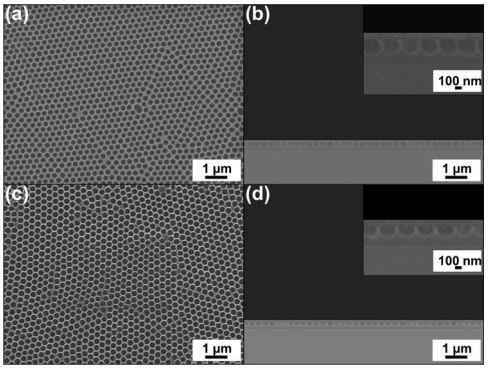

Figure 7. (a) Top-view SEM image of a three-quarter-spherical hole array prepared using a 300 nm silica colloidal suspension with a colloid volume fraction of 71 vol %. (b) Cross-sectional SEM image of the sandwich structure fabricated using the three-quarter-spherical hole array, while the thickness ratio of each layer is adjusted to be 1:2:1 (φ = 0.34). (c) Top-view SEM image of a hemispherical hole array prepared using a 300 nm silica colloidal suspension with a colloid volume fraction of 79 vol %. (d) Cross-sectional SEM image of the sandwich structure fabricated using the hemispherical hole array, while the thickness ratio of each layer is adjusted to be 1:2:1 (φ = 0.30). Inserts showing the corresponding magnified cross-sectional SEM images.

Moreover, it is apparent that a three-quarter-spherical hole array can be obtained by using the colloidal suspension with a colloid volume fraction of 71 vol %, while a hemispherical hole array is created as the colloid volume fraction reaches 79 vol %. The long-range arrangement of the holes is clearly evident even across distinct regions of the specimen, indicating the high uniformity and structural integrity of the hole array over a large area (Figure S17). The hole arrays are then employed as

https://doi.org/10.1021/acsami.5c15999
ACS Appl. Mater. Interfaces 2025, 17, 55294–55306

Table 5. Young's Moduli, Hardness, and Dissipation Energies of Taiwan Rhinoceros Beetle-Inspired Sandwich Structures, Templated from 300 nm Silica Colloidal Crystals[a]

Sample	Porosity	Experimental / Theoretical Young's Modulus (GPa)	Hardness (GPa)	Dissipation Energy (10^{-12} J)
1:2:1(Solid) 	0	3.49 ± 0.03 / NA	0.12 ± 0.01	6.72 ± 0.17
1:2:1 (Spherical Pores) 	0.30	2.31 ± 0.14 / 2.17	0.08 ± 0.01	10.96 ± 0.17
1:2:1 (Three-Quarter Spherical Pores) 	0.34	2.50 ± 0.21 / 2.03	0.09 ± 0.01	9.82 ± 0.19
1:2:1 (Hemispherical Pores) 	0.30	2.75 ± 0.27 / 2.17	0.11 ± 0.01	7.16 ± 0.21

[a]The structural geometries of the pores are controlled to be spherical, three-quarter-spherical, and hemispherical in shape, while the layer thickness ratios are adjusted to be 1:2:1.

structural supports to build bioinspired sandwich structures, of which their layer thickness ratios are determined to be 1:2:1. Compared with the mechanical behaviors of the sandwich structure embedded with spherical pores, the sandwich structure composed of three-quarter-spherical pores exhibits a higher indentation hardness of 0.09 ± 0.01 GPa, a higher Young's modulus of 2.50 ± 0.21 GPa, and a lower dissipation energy of 9.82 ± 0.19 pJ (Figure S18 and Table 5). To develop a clearer insight, the corresponding porosity (φ) is calculated as follows:

$$\varphi = \frac{V_{air}}{V_{total}} = \frac{\frac{1}{2}\left(\int_0^r \int_{\pi/3}^{\pi} \int_0^{2\pi} r^2 \sin\theta \, d\varphi \, d\theta \, dr + \frac{1}{3} \times \pi \times \left(\frac{\sqrt{3}}{2}r\right)^2 \times \frac{r}{2}\right)}{\frac{\sqrt{3}}{4}(2r)^2 \times h} = \frac{3\sqrt{3} \times \pi \times r}{16 \times h} \quad (9)$$

where r and h refer to the radius of the silica templates (150 nm) and the thickness of the whole sandwich structure (450 nm), respectively. It is perceptible that this sandwich structure possesses a larger φ (0.34), and hence shall perform an improved impact resistance in accordance with the Gibson-Ashby model.[55] Unfortunately, these three-quarter-spherical pores are contorted severely in response to the load of 100 μN; therefore, the impact energy cannot be dissipated effectively. As one would anticipate, the sandwich structure embedded with hemispherical pores presents an even lower dissipation energy (7.16 ± 0.21 pJ), resulting from the integration of even more deficient pores and thinner layers. Although the employment of three-quarter-spherical or hemispherical pores can reduce the light scattering, generating an enhanced antireflection functionality (Figure S19 and Table S5), it is recognized that these nonspherical pores give rise to a diminished impact resistance.

This research further studies the dependence of dissipation energy and average transmittance in the visible spectrum on the porosity of the as-engineered bioinspired sandwich structures. As shown in Figure S20, the higher porosity identified within the sandwich structure allows the structure to be deformed more easily in response to external stress, and hence facilitates the impact energy dissipation. In addition, the increasing porosity leads to an enhancement in average optical transmittance as well. Nevertheless, it is evident that the sandwich structures templated from 500 nm silica spheres display lower average transmittances, which are attributed to the light scattering from the resulting pores. As a summary, optimal impact resistances with an antireflection functionality are found on the sandwich structure comprised of a 150 nm-thick poly(ETPTA)/poly(EGDA) (20:1) upper layer, a 300 nm-thick poly(ETPTA)/poly(EGDA) (1:3) layer embedded with 300 nm spherical pores, and a 150 nm-thick poly(ETPTA)/poly(EGDA) (20:1) lower layer. A Taber abrasion-resistance test according to the ASTM D 1044 method is further applied to determine the mechanical durability of this specimen. As displayed in Figure S21, the corresponding optical reflectance and transmittance remain well-preserved throughout 300 abrasion cycles. In contrast, its intrinsic antireflective characteristics are significantly degraded after 500 abrasion cycles, resulting from the presence of pronounced surface scratches. The mechanical durability is competitive with that of commercial antireflection coatings.[2,6] Importantly, it is evidenced that the antireflection performance can even be maintained for up to half a year under ambient conditions of 25 °C and an average relative humidity of 70% (Figure S22).

Despite all this, these porous structures are observed to be squeezed and distorted in shape after a nanoindentation test with a maximum load of 100 μN (Figure 8(a)). The reduced porosity inevitably brings about a decline in impact resistance, accompanied by a degraded antireflection performance. It is of vital importance that the poly(ETPTA)/poly(EGDA) (1:3) copolymer exhibits room-temperature shape memory behaviors. Owing to this unique behavior, the corresponding structural configuration can be reversibly converted between temporarily deformed and original states in the ambient environment (Figure S23). Upon rinsing the deformed sandwich structure with low-surface-tension liquids, the poly(ETPTA)/poly(EGDA) (1:3) copolymer layer can absorb the liquid molecules, and undergo a substantial swelling. This swelling significantly relaxes the stretched copolymer chains, enabling these squeezed pores to recover their original configurations through the utilization of evaporation-induced capillary forces. As evidenced in Figure 8(b)-(d), the structural recovery can be triggered by drying out ethanol within the

https://doi.org/10.1021/acsami.5c15999
ACS Appl. Mater. Interfaces 2025, 17, 55294−55306

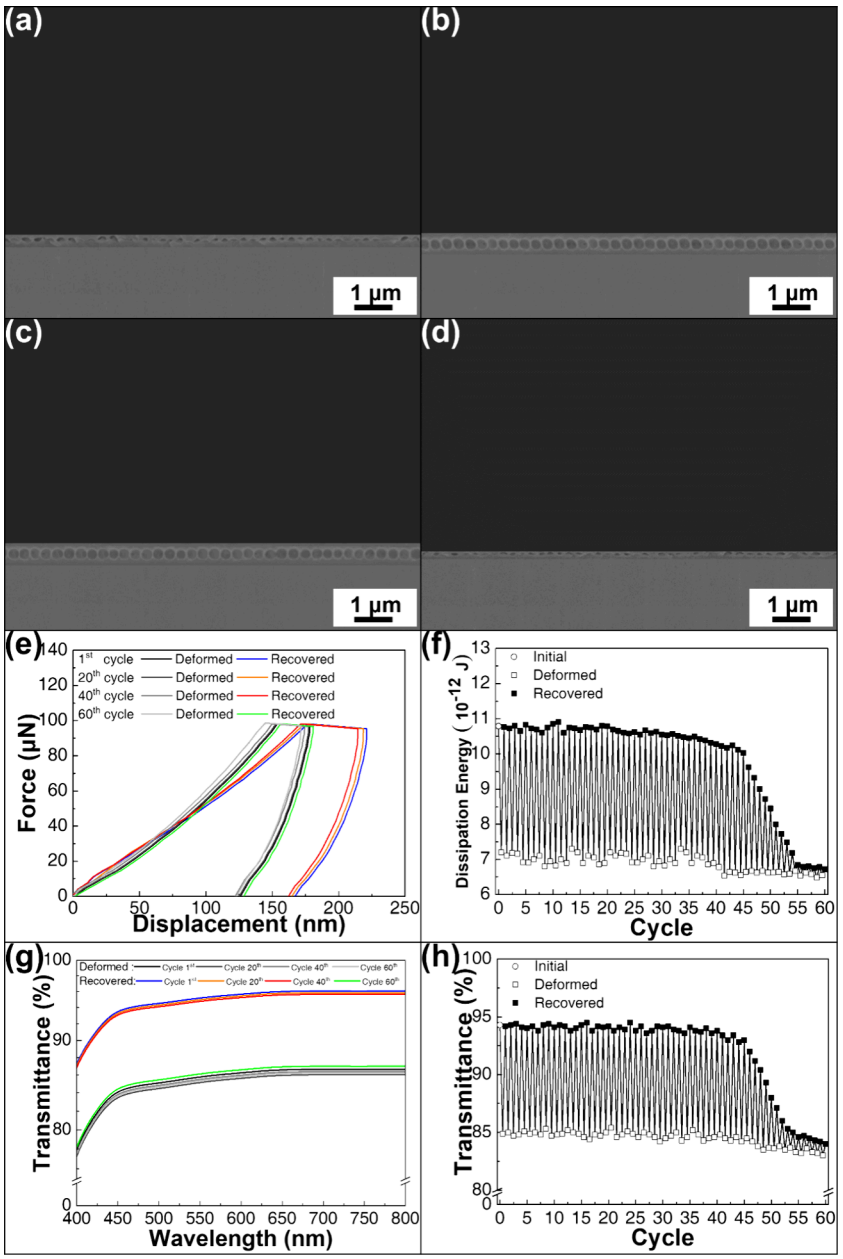

Figure 8. Cross-sectional SEM images of (a) the temporarily deformed Taiwan rhinoceros beetle-inspired sandwich structures and the recovered structures after the (b) 20th, (c) 40th, and (d) 60th deformation/recovery cycles. The sandwich structure is templated from 300 nm silica colloidal crystals, while the thickness ratio of each layer is adjusted to be 1:2:1 (φ = 0.30). (e) Load−displacement curves obtained from nanoindentation tests with maximum loads of 100 μN on the temporarily deformed and recovered sandwich structures after the 1st, 20th, 40th, and 60th deformation/recovery cycles. (f) Dissipation energies of the temporarily deformed and recovered sandwich structures in the deformation/recovery cycles. The sample is replaced after each cycle. (g) Normal-incidence optical transmission spectra of the temporarily deformed and recovered sandwich structures after the 1st, 20th, 40th, and 60th deformation/recovery cycles. (h) Average transmittances of the temporarily deformed and recovered sandwich structures in the deformation/recovery cycles.

submicrometer-scale structure in a few seconds at 25 °C for at least 40 deformation/recovery cycles. In the structural transformation cycles, the sandwich structure is redeformed immediately after the structural recovery. Importantly, the bioinspired sandwich structure, thereupon, regains its inherent antireflective and impact resistances. Although the structural configuration is incrementally distorted, it is validated that the dissipation energy of the recovered sandwich structure, even after 40 deformation/recovery cycles, is comparable to that of the original one (Figure 8(e) and (f)). The results further reveal that the adoption of poly(ETPTA)/poly(EGDA) (1:3) porous structures renders a straightforward strategy for designing and building recoverable impact-resistant structures. Crucially, the average transmittance of the sandwich structure is merely reduced from 94.7 to 94.3% over 40 deformation/recovery cycles (Figure 8(g) and (h)), indicating that the corresponding antireflection performance can be restored as well. Owing to the antireflection functionality, the bioinspired sandwich structure-coated cover glass is highly transparent under white light illumination (Figure S24). Interestingly, a "double heart" pattern can be printed on the stimuli-responsive sandwich structure by applying a contact pressure using a

https://doi.org/10.1021/acsami.5c15999
ACS Appl. Mater. Interfaces 2025, 17, 55294−55306

rubber stamp. The increase in the contact pressure causes the structure to be deformed more severely, and hence the patterns reveal themselves more distinctly as the contact pressure increases from 0.1 to 1.0 MPa. As predicted, the pattern is fully erased through ethanol drying. Most importantly, it is ascertained that the impact resistances and antireflective behaviors of the bioinspired sandwich structure-coated substrate in existence can be determined by its appearance.

To assess the practical versatility, the Taiwan rhinoceros beetle-inspired sandwich structure is engineered on a commercial PET film following the fabrication procedures detailed above. For this particular instance, the sandwich structure is templated from 300 nm silica colloidal crystals, and the thickness ratio of each layer is adjusted to be 1:2:1 (φ = 0.30). As displayed in Figure S25, reflected glare appears on a bare PET film under natural lighting, caused by the refractive index disparity between air and the PET substrate. In comparison, the sandwich structure establishes a refractive index gradient at the air/PET interface. Accordingly, the sandwich structure-coated PET film is highly transparent, allowing the beetle image underneath to be observed clearly. The antireflective properties are further verified by conducting the normal-incidence optical reflection and transmission spectra of these specimens. It is evidenced that the application of the bioinspired sandwich structure results in a reduction of the average reflectance in the visible spectrum by approximately 2.6%, accompanied by an increase in average transmittance of about 2.5%, which is competitive with the antireflection performance found on the sandwich structure-coated glass substrate. In sharp contrast, the sandwich structure-coated PET film turns milky in appearance after applying a contact pressure of 1.0 MPa. The opaque appearance arises from light scattering induced by distortions within the sandwich structure. Furthermore, the temporarily deformed structure and the corresponding appearance can be fully restored through an ethanol drying procedure. Importantly, the structural configuration and optical behaviors remain unchanged across the sandwich structure-coated PET film (Figure S26). Furthermore, the consistency of the corresponding impact resistances is validated. Compared with the dissipation energy of a bare PET film (7.32 ± 0.12 pJ), the dissipation energy can be distinctly enhanced on the sandwich structure-coated PET film (10.79 ± 0.17 pJ). The results provide compelling evidence of the scalability potential of this proposed fabrication methodology.

CONCLUSIONS

In summary, a nonlithography-based methodology is developed to assemble Taiwan rhinoceros beetle-inspired sandwich structures, which are supported by shape memory polymer-based porous structures. The bioinspired sandwich structures possess small refractive indices that lie between those of air and glass, and hence can be utilized to suppress light reflections occurring at the air/glass interface. It is worth noting that the employment of subwavelength-scale pores greatly reduces the light scattering, leading to an improved antireflection functionality. Although these pores are severely squeezed upon applying contact pressures onto the sandwich structures, the structural deformation allows the impact energies to be dissipated more effectively. In addition, it is empirically demonstrated that the impact resistance can be enhanced by introducing an increased porosity within the sandwich structure. Importantly, these temporarily deformed pores are capable of recovering their original structural geometries through drying out ethanol under ambient conditions, thereby restoring the corresponding impact resistances and antireflective characteristics. The reversible structural transitions undoubtedly create novel dimensions for a variety of promising applications, including optical lenses, wearable devices, flexible displays, aerospace optical domes, optical communication components, and medical endoscopes.

ASSOCIATED CONTENT

Supporting Information

The Supporting Information is available free of charge at https://pubs.acs.org/doi/10.1021/acsami.5c15999.

Porosities, Young's moduli, hardnesses, and dissipation energies of a Taiwan rhinoceros beetle. Schematic illustration of the templating procedures for engineering Taiwan rhinoceros beetle-inspired structures with varied structural configurations. Photographic images, SEM images, load−displacement curves, normal-incidence optical reflection spectra, and normal-incidence optical transmission spectra of featureless copolymer layer-coated glass substrates, the bioinspired structure-coated glass substrates, and the bioinspired structure-coated PET substrates. Porosities, Young's moduli, hardnesses, dissipation energies, average reflectances, and average transmittances of the bioinspired structure-coated specimens. (PDF)

AUTHOR INFORMATION

Corresponding Authors

Hui-Ping Tsai − *Department of Civil Engineering, National Chung Hsing University, Taichung 40227, Taiwan*; Email: huiping.tsai@nchu.edu.tw

Hongta Yang − *Department of Chemical Engineering, National Chung Hsing University, Taichung 40227, Taiwan*; orcid.org/0000-0002-5822-1469; Email: hyang@dragon.nchu.edu.tw

Authors

Bo-Han Zeng − *Department of Chemical Engineering, National Chung Hsing University, Taichung 40227, Taiwan*

Shang-Hsuan Lu − *Department of Chemical Engineering, National Chung Hsing University, Taichung 40227, Taiwan*

Hsiang-Wen Hsueh − *Department of Chemical Engineering, National Chung Hsing University, Taichung 40227, Taiwan*

Cai-Yin Fang − *Department of Chemical Engineering, National Chung Hsing University, Taichung 40227, Taiwan*

Shin-Hua Lin − *Department of Chemical Engineering, National Chung Hsing University, Taichung 40227, Taiwan*

Zi-Xuan Chen − *Department of Chemical Engineering, National Chung Hsing University, Taichung 40227, Taiwan*

Ya-Lien Cheng − *Department of Chemical Engineering, National Chung Hsing University, Taichung 40227, Taiwan*

Yu-Fang Wang − *Department of Chemical Engineering, National Chung Hsing University, Taichung 40227, Taiwan*

Chia-Feng Lin − *Department of Materials Science & Engineering, National Chung Hsing University, Taichung 40227, Taiwan*; orcid.org/0000-0002-1743-4337

Rong-Ho Lee − *Department of Chemical Engineering, National Chung Hsing University, Taichung 40227, Taiwan*

Complete contact information is available at: https://pubs.acs.org/10.1021/acsami.5c15999

https://doi.org/10.1021/acsami.5c15999
ACS Appl. Mater. Interfaces 2025, 17, 55294−55306

Author Contributions

B.-H.Z. and S.-H.L. contributed equally.

Notes

The authors declare no competing financial interest.

■ ACKNOWLEDGMENTS

This research is financially supported by grant number NSTC 112-2221-E-005-006-MY3 under the National Science and Technology Council. Acknowledgments are also made to the *i*-Center for Advanced Science and Technology of National Chung-Hsing University and the Innovative Center on Sustainable Negative-Carbon Resources under the Ministry of Education.

■ REFERENCES

(1) Shanmugam, N.; Pugazhendhi, R.; Madurai Elavarasan, R.; Kasiviswanathan, P.; Das, N. Anti-Reflective Coating Materials: A Holistic Review from PV Perspective. *Energies* **2020**, *13* (10), 2631.

(2) Law, A. M.; Jones, L. O.; Walls, J. M. The Performance and Durability of Anti-Reflection Coatings for Solar Module Cover Glass—A Review. *Sol. Energy* **2023**, *261*, 85−95.

(3) Selj, J.; Mongstad, T.; Søndenå, R.; Marstein, E. Reduction of Optical Losses in Colored Solar Cells with Multilayer Antireflection Coatings. *Sol. Energy Mater. Sol. Cells.* **2011**, *95* (9), 2576−2582.

(4) Pfeiffer, K.; Schulz, U.; Tünnermann, A.; Szeghalmi, A. Antireflection Coatings for Strongly Curved Glass Lenses by Atomic Layer Deposition. *Coatings* **2017**, *7* (8), 118.

(5) Fluder, G.; Kowalik, A.; Rojek, A.; Sobczyk, A.; Choromański, Z.; Krężel, J.; Józwik, M. Analysis of the Influence of Antireflective Coatings on the Diffraction Efficiency of Diffractive Optical Elements. *Opt. Express* **2021**, *29* (9), 13025−13032.

(6) Buskens, P.; Burghoorn, M.; Mourad, M. C. D.; Vroon, Z. Antireflective Coatings for Glass and Transparent Polymers. *Langmuir* **2016**, *32* (27), 6781−6793.

(7) Guo, Z.; Zhao, H.; Zhao, W.; Wang, T.; Kong, D.; Chen, T.; Zhang, X. High-Quality Hollow Closed-Pore Silica Antireflection Coatings Based on Styrene−Acrylate Emulsion@ Organic−Inorganic Silica Precursor. *ACS Appl. Mater. Interfaces.* **2016**, *8* (18), 11796−11805.

(8) Zhang, X.; Lan, P.; Lu, Y.; Li, J.; Xu, H.; Zhang, J.; Lee, Y.; Rhee, J. Y.; Choy, K.-L.; Song, W. Multifunctional Antireflection Coatings Based on Novel Hollow Silica−Silica Nanocomposites. *ACS Appl. Mater. Interfaces.* **2014**, *6* (3), 1415−1423.

(9) Lei, H.; Wang, Y.; Zhang, B.; Li, X. Design of a Novel Anti-Reflective Coating with Ultra-Low Reflectance Based on Resin-Anchored Hollow Silica Strategy. *Prog. Org. Coat.* **2024**, *186*, No. 108033.

(10) Osman, M. A.; Atallah, A.; Suter, U. W. Influence of Excessive Filler Coating on the Tensile Properties of LDPE−Calcium Carbonate Composites. *Polymer* **2004**, *45* (4), 1177−1183.

(11) Shen, A. Q.; Gleason, B.; McKinley, G. H.; Stone, H. A. Fiber Coating with Surfactant Solutions. *Phys. Fluids.* **2002**, *14* (11), 4055−4068.

(12) Ee, H.-S.; Kang, J.-H.; Brongersma, M. L.; Seo, M.-K. Shape-Dependent Light Scattering Properties of Subwavelength Silicon Nanoblocks. *Nano Lett.* **2015**, *15* (3), 1759−1765.

(13) Zhong, B.; Guo, W. L.; He, D. Y.; Xing, Z. G.; Huang, Y. F.; Lv, X. R. Anti-Reflective Properties of Butterfly-Wing-Micro-Nano Structures in the Infrared Band. *Opt. Laser Technol.* **2024**, *169*, No. 109863.

(14) Li, P. C.; Chen, H. Y.; Chiang, K. T.; Yang, H. Reversible Embroidered Ball-Like Antireflective Structure Arrays Inspired by Leafhopper Wings. *J. Colloid Interface Sci.* **2021**, *599*, 119−129.

(15) Liu, F.; Sun, Y.; Wang, Z.; Li, B.; Niu, S.; Zhang, J.; Han, Z.; Ren, L. Reversible Antireflection Materials Inspired by Cicada Wings for Anticounterfeit and Photovoltaic Cells. *ACS Appl. Mater. Interfaces* **2024**, *16* (45), 63049−63058.

(16) Chen, R. Y.; Lai, C. J.; Chen, Y. J.; Wu, M. X.; Yang, H. Omnidirectional Unidirectional Antireflection-Switchable Structures Inspired by Dragonfly Wings. *J. Colloid Interface Sci.* **2022**, *610*, 246−257.

(17) Novikova, A.; Katiyi, A.; Karabchevsky, A. Nature-Inspired Anti-Reflective Texturization for Solar Energy Applications. *Adv. Mater. Technol.* **2024**, *9* (2), No. 2301128.

(18) Wu, T.; Wang, G.; Li, J.; Yan, K. Investigation on Gear Rolling Process Using Conical Gear Rollers and Design Method of the Conical Gear Roller. *J. Mater. Process Technol.* **2018**, *259*, 141−149.

(19) Sim, Y. H.; Yun, M. J.; Cha, S. I.; Seo, S. H.; Lee, D. Y. Improvement in Energy Conversion Efficiency by Modification of Photon Distribution within the Photoanode of Dye-Sensitized Solar Cells. *ACS Omega* **2018**, *3* (1), 698−705.

(20) Chen, H. Y.; Chiang, K. T.; Ye, Y. Z.; Lin, K. Y. A.; Yang, H. Tunable Antireflective Characteristics Enabled by Small Yellow Leafhopper-Inspired Soccer Ball-Shaped Structure Arrays. *J. Taiwan Inst. Chem. Eng.* **2022**, *136*, No. 104407.

(21) Xie, Z.; Stoesser, T. Two-Phase Flow Simulation of Breaking Solitary Waves Over Surface-Piercing and Submerged Conical Structures. *Ocean Eng.* **2020**, *213*, No. 107679.

(22) Kovačič, M.; Will, P.-A.; Lipovšek, B.; Topič, M.; Lenk, S.; Reineke, S.; Krč, J. Coupled Optical Modeling for Optimization of Organic Light-Emitting Diodes with External Outcoupling Structures. *ACS Photonics* **2018**, *5* (2), 422−430.

(23) Kong, X.; Fan, X.; Wang, Y.; Luo, Y.; Chen, Y.; Wu, T.; Chen, Z.; Lin, Y.; Wang, S. Recent Advances of Photolithography Patterning of Quantum Dots for Micro-Display Applications. *Nano Mater. Sci.* **2025**, *7* (1), 49−64.

(24) Liu, W.; Wang, J.; Xu, X.; Zhao, C.; Xu, X.; Weiss, P. S. Single-Step Dual-Layer Photolithography for Tunable and Scalable Nanopatterning. *ACS Nano* **2021**, *15* (7), 12180−12188.

(25) Yang, G. G.; Choi, H. J.; Li, S.; Kim, J. H.; Kwon, K.; Jin, H. M.; Kim, B. K.; Kim, S. O. Intelligent Block Copolymer Self-Assembly towards IoT Hardware Components. *Nat. Rev. Electr. Eng.* **2024**, *1*, 124−138.

(26) You, D. W.; Yoon, J.; Kim, S.; Yang, G. G.; Lee, C. W.; Shin, J.; Hong, S.; Kim, J. W.; Kim, S. O. Bioinspired Deformable Antireflective Materials by Block Copolymer Self-Assembly. *ACS Appl. Mater. Interfaces* **2025**, *17*, 24610−24619.

(27) Kojima, W.; Hidaka, K.; Koizumi, S.; Murayama, Y.; Nakata, T. Hard Exoskeleton of Beetles as Armour Against Avian Predators. *Anim. Behav.* **2024**, *218*, 163−172.

(28) Cai, Z.-B.; Li, Z.-Y.; Ding, Y.; Zheng, J.; Liu, J.-H.; Zhou, Z.-R. Preparation and Impact Resistance Performance of Bionic Sandwich Structure Inspired from Beetle Forewing. *Compos. B Eng.* **2019**, *161*, 490−501.

(29) Zhou, M.; Huang, D. Q.; Su, X. L.; Zhong, J. T.; Hassanein, M. F.; An, L. Analysis of Microstructure Characteristics and Mechanical Properties of Beetle Forewings, Allomyrina Dichotoma. *Mater. Sci. Eng. C-Mater. Biol. Appl.* **2020**, *107*, 110317.

(30) Yu, M.; Hermann, I.; Dai, Z. D.; Gitis, N. Mechanical and Frictional Properties of the Elytra of Five Species of Beetles. *J. Bionic Eng.* **2013**, *10* (1), 77−83.

(31) Dai, Z.; Yang, Z. Macro-/Micro-Structures of Elytra, Mechanical Properties of the Biomaterial and the Coupling Strength between Elytra in Beetles. *J. Bionic Eng.* **2010**, *7* (1), 6−12.

(32) Chen, J. X.; Huang, J. Y.; Pan, L. C.; Zhao, T. D.; Zhang, X. M.; Lin, H. W. The 3D Lightweight Structural Characteristics of the Beetle Forewing: Verification. *Structures* **2021**, *33*, 2943−2949.

(33) Lomakin, J.; Huber, P. A.; Eichler, C.; Arakane, Y.; Kramer, K. J.; Beeman, R. W.; Kanost, M. R.; Gehrke, S. H. Mechanical Properties of the Beetle Elytron, a Biological Composite Material. *Biomacromolecules* **2011**, *12* (2), 321−335.

(34) Borah, R.; Raj, A. K.; Minja, A. C.; Verbruggen, S. W. A Review on Self-Assembly of Colloidal Nanoparticles into Clusters, Patterns, and Films: Emerging Synthesis Techniques and Applications. *Small Methods* **2023**, *7* (6), 32.

https://doi.org/10.1021/acsami.5c15999
ACS Appl. Mater. Interfaces 2025, 17, 55294−55306

(35) Wang, H. Y.; Li, H.; Gu, P.; Huang, C. L.; Chen, S. B.; Hu, C. L.; Lee, E.; Xu, J. P.; Zhu, J. T. Electric, Magnetic, and Shear Field-Directed Assembly of Inorganic Nanoparticles. *Nanoscale* **2023**, *15* (5), 2018−2035.
(36) Suh, Y.; Pham, Q.; Shao, B. W.; Won, Y. The Control of Colloidal Grain Boundaries Through Evaporative Vertical Self-Assembly. *Small* **2019**, *15* (12), 9.
(37) Wang, H. B.; Chen, W.; Chen, B.; Jiao, Y.; Wang, Y.; Wang, X. P.; Du, X. C.; Hu, Y.; Lv, X. X.; Zeng, Y. S. Interfacial Capillary-Force-Driven Self-Assembly of Monolayer Colloidal Crystals for Super-sensitive Plasmonic Sensors. *Small* **2020**, *16* (8), 9.
(38) Liu, S.; Zhao, H. M.; Lyu, Y.; Wu, T.; Zhai, F.; Zhang, Y.; Ji, Z. Y.; Wang, X. L. Grayscale Stereolithography 3D Printing of Shape Memory Polymers for Dual Information Encryption Based on Reconfigurable Geometry and Tunable Optics. *Chem. Eng. J.* **2024**, *487*, 150552.
(39) Yang, G.; Li, H. Q.; Xing, R. Q.; Lv, M. D.; Ma, C. Q.; Yan, J.; Zhuang, X. P. Thermal-Triggered "On-Off" Switchable Triboelectric Nanogenerator Based on Two-Way Shape Memory Polymer. *Adv. Funct. Mater.* **2023**, *33* (13), 11.
(40) Wang, L.; Zhang, F.; Liu, Y.; Leng, J. Shape Memory Polymer Fibers: Materials, Structures, and Applications. *Adv. Fiber Mater.* **2022**, *4* (1), 5−23.
(41) Luo, L.; Zhang, F.; Wang, L.; Liu, Y.; Leng, J. Recent Advances in Shape Memory Polymers: Multifunctional Materials, Multiscale Structures, and Applications. *Adv. Funct. Mater.* **2024**, *34* (14), No. 2312036.
(42) Tang, Z.; Gong, J.; Cao, P.; Tao, L.; Pei, X.; Wang, T.; Zhang, Y.; Wang, Q.; Zhang, J. 3D Printing of a Versatile Applicability Shape Memory Polymer with High Strength and High Transition Temperature. *Chem. Eng. J.* **2022**, *431*, No. 134211.
(43) Stöber, W.; Fink, A.; Bohn, E. Controlled Growth of Monodisperse Silica Spheres in the Micron Size Range. *J. Colloid Interface Sci.* **1968**, *26* (1), 62−69.
(44) Gao, X.; Hong, D.; Paranjape, H. M.; Zhang, W.; Anderson, P. M. Berkovich Indentation and the Oliver-Pharr Method for Shape Memory Alloys. *Int. J. Mech. Sci.* **2024**, *270*, No. 109077.
(45) Zhang, Y.; Needleman, A. Characterization of Plastically Compressible Solids Via Spherical Indentation. *J. Mech. Phys. Solids.* **2021**, *148*, No. 104283.
(46) Yu, M.; Hermann, I.; Dai, Z.; Gitis, N. Mechanical and Frictional Properties of the Elytra of Five Species of Beetles. *J. Bionic Eng.* **2013**, *10* (1), 77−83.
(47) Dai, Z.; Yang, Z. Macro-Structures of Elytra, Mechanical Properties of the Biomaterial and the Coupling Strength between Elytra in Beetles. *J. Bionic Eng.* **2010**, *7* (1), 6−12.
(48) Fumina, A.; Speshilova, A.; Belyanov, I.; Endiiarova, E.; Osipov, A. Technique for Creating 3D Ordered Colloidal Crystals with Hexagonal Close Packing and Uniform Thickness over a Large Area. *J. Phys. Chem. B* **2025**, *129* (2), 750−762.
(49) Fang, Y.; Ni, Y.; Leo, S.-Y.; Taylor, C.; Basile, V.; Jiang, P. Reconfigurable Photonic Crystals Enabled by Pressure-Responsive Shape-Memory Polymers. *Nat. Commun.* **2015**, *6* (1), 7416.
(50) Wu, M.-X.; Hsueh, H.-W.; Lu, S.-H.; Zeng, B.-H.; Huang, Y.-W.; Fang, C.-Y.; Yeh, S.-Y.; Hsieh, S.-H.; Yang, H. Self-Assembly of Impact-Resistant and Shape-Recoverable Structures Inspired by Taiwan Rhinoceros Beetles. *ACS Appl. Mater. Interfaces* **2025**, *17* (16), 24630−24643.
(51) Xie, Y.; Sengupta, M.; Habte, A.; Andreas, A. The "Fresnel Equations" for Diffuse Radiation on Inclined Photovoltaic Surfaces (FEDIS). *Renew. Sustain. Energy Rev.* **2022**, *161*, No. 112362.
(52) Liu, B.-T.; Yeh, W.-D. Reflective Properties of Nanoparticle-Arrayed Surfaces. *Thin Solid Films* **2010**, *518* (21), 6015−6021.
(53) Du, H. Mie-Scattering Calculation. *Appl. Opt.* **2004**, *43* (9), 1951−1956.
(54) Gaylord, T. K.; Moharam, M. G. Analysis and Applications of Optical Diffraction by Gratings. *IEEE* **1985**, *73* (5), 894−937.
(55) Jalali, S. K.; Beigrezaee, M. J.; Misseroni, D.; Pugno, N. M. A Modified Gibson-Ashby Model for Functionally Graded Lattice Structures. *Mech. Mater.* **2024**, *188*, No. 104822.

https://doi.org/10.1021/acsami.5c15999
ACS Appl. Mater. Interfaces 2025, 17, 55294−55306